Single-molecule force stability of the SARS-CoV-2–ACE2 interface in variants-of-concern

Magnus S. Bauer[1, 2, †], **Sophia Gruber**[1, †], **Adina Hausch**[1, 3, †], **Marcelo C.R. Melo**[4, †], **Priscila S.F.C. Gomes**[4, †], **Thomas Nicolaus**[1], **Lukas F. Milles**[5,6], **Hermann E. Gaub**[1, *], **Rafael C. Bernardi**[4, *], **and Jan Lipfert**[1, 7, *]

[1] Department of Physics and Center for NanoScience (CeNS), LMU Munich, 80799 Munich, Germany;
[2] Department of Chemical Engineering, Stanford University, Stanford, CA 94305, USA;
[3] Center for Protein Assemblies, TUM School of Natural Sciences, Technical University of Munich, Germany;
[4] Department of Physics, Auburn University, Auburn, AL 36849, USA;
[5] Department of Biochemistry, University of Washington, Seattle, WA 98195, USA;
[6] Institute for Protein Design, University of Washington, Seattle, WA 98195, USA;
[7] Department of Physics and Debye Institute for Nanomaterials Science, Utrecht University, 3584 CC Utrecht, The Netherlands;

[†] These authors contributed equally.
* Joint corresponding authorship.

ABSTRACT

Viruses mutate under a variety of selection pressures, allowing them to continuously adapt to their hosts. Mutations in SARS-CoV-2 have shown effective evasion of population immunity and increased affinity to host factors, in particular to the cellular receptor ACE2. However, in the dynamic environment of the respiratory tract forces act on the binding partners, which raises the question whether not only affinity, but also force-stability of the SARS-CoV-2:ACE2 bond, might be a selection factor for mutations. Here, we use magnetic tweezers (MT) to study the effect of amino acid substitutions in variants of concern (VOCs) on RBD:ACE2 force-stability and bond kinetics with and without external load. We find higher affinity for all VOCs compared to wt, in good agreement with previous affinity measurements in bulk. In contrast, Alpha is the only VOC that shows significantly higher force stability compared to wt. Investigating the RBD:ACE2 interactions with molecular dynamics simulations, we are able to rationalize the mechanistic molecular origins of this increase in force-stability. Our study emphasizes the diversity of contributions to the assertiveness of variants and establishes force-stability as one of several factors for fitness. Understanding fitness-advantages opens the possibility for prediction of likely mutations allowing rapid adjustment of therapeutics, vaccination, and intervention measures.

INTRODUCTION

Viruses constantly adapt to their hosts through genomic changes. While many mutations are silent or inviable, some result in increased fitness by increasing intrinsic transmissibility or evasion of population immunity. Better adaptation and higher transmissibility enable new variants to supersede existing ones, as it was observed by the emergence and rapid spread of variants of concern (VOC) of SARS-CoV-2 (Supplementary Figure S1). Adaptations associated with increased fitness of SARS-CoV-2 often go along with higher affinity to host factors (*1, 2*). Nonetheless, the attachment of SARS-CoV-2 to the human ACE2 receptor occurs within the dynamic environment of the respiratory tract, where external forces generated by breathing, coughing, and ciliary beating-mediated mucus clearing (*3, 4*) continuously challenge the attachment process (Figure 1A). It is crucial to recognize that, for a successful infection, not only affinity but also stability under force of the viral attachment to the host plays a critical role (5-11). Single-molecule measurements have demonstrated that SARS-CoV-2 VOCs exhibit higher binding frequencies (9, 11, 12), greater avidity (13), and extended bound lifetimes (9, 11, 13) compared to the wild-type virus, suggesting differences in mechanical stability among variants.

Despite these findings, the variation in force-stability across various VOCs and its potential correlation with viral transmissibility remain unclear. In this study, we employ a highly sensitive single-molecule assay designed to simulate the natural force-exposure experienced during infection, enabling the examination of SARS-CoV-2 attachment to ACE2 under load. Our approach uses a fusion protein construct that features the receptor binding domain (RBD) from the SARS-CoV-2 spike protein coupled to the ACE2 ectodomain via a flexible peptide linker with molecular handles suitable for attachment in magnetic tweezers (MT; Figure 1B-D) (*14*). Coupling in MT enables us to probe the mechanical strength and dynamics of the RBD:ACE2 interaction under precisely defined forces, with very high force resolution (*14-20*) (Figure 1). Using our single-molecule assay, we characterize the interaction of SARS-CoV-2 wild type and VOC constructs with ACE2. Our assay enables direct measurements of force-stability, and reveals significant differences between the VOCs and we identify the amino acid substitutions responsible for the changes. In addition to force-stability, we find that by extrapolating bond lifetimes

to zero force, we can quantitatively compare to and reproduce equilibrium affinity constants measured in bulk. Using molecular dynamics (MD) simulations, we identify key residues that stabilize the RBD:ACE2 interface and calculate the correlation between their movements. Aggregating the individual correlations from MD simulations into a new total correlation metric, we are able to accurately reproduce the experimentally determined relations in force-stabilities. Thus, we can experimentally determine differences in the force-stability between different VOCs using MT and elucidate their molecular origin with the help of MD simulations. Correlating our results to observations from epidemiology, we suggest that increased force-stability of the ACE2:RBD interface can increase intrinsic transmissibility. We anticipate that taking into account force-stability will aid predictions of future variants of concern.

RESULTS AND DISCUSSION

Comparing the force stability of the SARS-CoV-2 interaction with ACE2 for VOCs

We design fusion protein constructs comprising the ectodomain of the human ACE2 receptor connected by a flexible polypeptide linker to the RBD of SARS-CoV-2 for both the wild type (wt) strain and the Alpha, Beta, Gamma, and Delta VOCs (Figure 1C,D; Table 1). We attach the tethered ligand constructs to a glass surface and a magnetic bead, respectively, using a previously established protocol based on specific peptide linkers (*14, 15, 20, 21*). Using MT, we probe the stability of the RBD:ACE2 interaction at varying levels of constant forces (Supplementary Figure S2). At high forces larger than 25 pN, ACE2 unfolds with a characteristic unfolding signature, which we use for each molecular construct probed in the MT to identify specific tethers (Supplementary Figure S3 and S4). At forces below 10 pN, where both protein domains are folded, the linker ensures that receptor and ligand remain in proximity upon dissociation, allowing them to re-bind (*14, 22-26*). We can thus study repeated (re-)binding and dissociation of the same SARS-CoV-2 RBD and ACE2 interaction under different forces (Figure 1E). At low forces (< 2 pN), we find the bond to be predominantly formed, while increasing the force leads to elongated periods where the binding partners are dissociated. Quantitating the force dependence of the RBD:ACE2 interaction gives access to both the equilibrium force stability and the dynamics of the interactions.

To characterize the force-stability and to, in particular, compare it across the different VOCs, we use $F_{1/2}$, the midpoint force, at which it is equally likely to find the tethered-ligand system in the bound or dissociated conformation (Figure 1F). We determine $F_{1/2}$ by fitting a two-state model to the fraction dissociated (f_{diss}) as a function of force (Figure 1G):

$$f_{diss}(F) = \frac{1}{(1+exp\,(-\Delta z(F-F_{\frac{1}{2}})/k_BT))} \quad (1)$$

where k_B is Boltzmann's constant and T the absolute temperature. $F_{1/2}$ and Δz are fitting parameters that represent the midpoint force and the distance between the two states along the pulling direction, respectively. The fraction dissociated is calculated for each plateau of constant force by dividing the time spent in the dissociated conformation by the total plateau time. Comparing F1/2 for the wt and the different VOCs, using otherwise identical constructs (Figure 2A,B and Supplementary Figure S5, S6), we find that the force-stability for the Alpha VOC is highly significantly larger than wt ($p = 5.2 \cdot 10^{-4}$, two-tailed t-test). In contrast, we observe no statistically significant difference between SARS-CoV-2 wt and Beta ($p > 0.80$), wt and Gamma ($p > 0.26$), or wt and Delta ($p > 0.99$). In addition to the naturally emerged VOCs, we tested individual amino acid substitutions and found that E484K slightly lowers $F_{1/2}$, albeit not statistically significantly, while K417N lowers the force stability highly significantly ($p = 4.5 \cdot 10^{-5}$).

Dynamics of the RBD:ACE2 interactions

To characterize the dynamics of the interactions, we determine the lifetimes of the dissociated and bound state as a function of force. The dwell time distributions are well described by single exponentials (Supplementary Figure S8). The resulting mean lifetimes, τ_{diss} and τ_{bound}, (Figure 1H, circles) exhibit an exponential force dependence (Figure 1H, lines). The intersection of the fitted lifetimes in the dissociated and bound state provides an alternative route to determine the midpoint force $F_{1/2}$ and we find excellent agreement in both the absolute values and differences across VOCs with the $F_{1/2}$ values determined using the two-state model (Equation 1; Supplementary Table T1).

Further, extrapolation of the fits to zero force, assuming a slip bond behavior with an exponential dependence of lifetime on force, yields lifetimes of the bond in the absence force (Figure 2C, Supplementary Table T1). The lifetimes of the dissociated state increase rapidly with increasing force for all constructs, which is expected as the peptide linker

extends under force, which in turn impedes bond re-formation (*14, 22, 27, 28*). Conversely, the lifetimes of the bound state τ_{bound} decrease with force for all VOCs. However, the force dependence of τ_{bound} differs for the different VOCs (Supplementary Figure S7). For Alpha, we find a higher τ_{bound} than for wt over the whole measured force range (Figure 2C), again indicating a higher force-stability of Alpha in this force range, in line with observation of a higher $F_{1/2}$ for Alpha. The other VOCs exhibit overall similar lifetimes in the bound state compared to wt under force, in line with their similar $F_{1/2}$ values.

Bond lifetimes at zero force predict affinities

The force-dependence of the bond lifetime (i.e. the slope in Figure 2C) varies considerably across the VOCs, leading to very different extrapolated lifetimes $\tau_{0,bound}$ and $\tau_{0,diss}$ in the absence of load. The lifetimes at zero force can be related to affinities: the ratio $\tau_{0,\,diss}/\tau_{0,\,bound}$ (or equivalently the ratio of the rates $k_{0,off}$ / $k_{0,on}$, which are the inverses of the lifetimes) define unimolecular equilibrium constants for the tethered ligand system $K_D^{TL} = \tau_{0,diss}/\tau_{0,bound}$ (Supplementary Figure S9). The K_D^{TL} are dimensionless, since both on- and off-rates for the tethered ligand systems are in units of 1/s. To compare K_D^{TL} to bulk binding measurements, we need to take into account that in standard solution assays, without a linker, the bimolecular equilibrium constant $K_{D,sol} = k_{off,sol} / k_{on,sol}$ has units of M, since while the off-rate $k_{off,sol}$ is directly comparable to $k_{0,off}$, the on-rate $k_{on,sol}$ is depending on the ligand concentration, with unit of 1/M·s.

Therefore, we normalize both the unimolecular equilibrium constant K_D^{TL} and the bimolecular dissociation constants $K_{D,sol}$ obtained using standard binding assays (*1, 2, 29-33*) (*3–9*) to the wt and compare across the VOCs (Figure 2D). We find good agreement between the affinities determined in our single-molecule assay by extrapolation to zero force and the values obtained from standard affinity measurements (Figure 2D). The good agreement between bulk affinity measurements in the absence of force and values from our assay suggest that our constant force magnetic tweezers measurements are close enough to equilibrium to probe the same (or at least a sufficiently similar) binding pathway as the free solution measurements. The exponential decrease in the lifetime of the bound state with increasing force (Figure 2C) and the good agreement between the force spectroscopy data extrapolated to zero force and the bulk binding measurements also implies that the RBD:ACE2 interaction is not a catch bond, but a “regular” slip bond, which

weakens under increasing force. However, the data also reveal a clear difference between affinities at zero force and stability under mechanical load: While all VOCs exhibit increased affinity compared to wt, only Alpha shows higher force stability. A clear difference between force stability and thermodynamic affinity has been seen for a range of molecular bonds (*34, 35*) and our findings suggest that force stability must be taken into account as an independent factor when assessing VOCs.

Molecular basis of different force stabilities across the VOCs

To provide a microscopic understanding of the observed differences in force stability, we performed all atom molecular dynamics (MD) simulations of the different RBD:ACE2 complexes. The structures of the VOCs were obtained by comparative modeling using Modeller (*36*), taking the SARS-CoV-2 wt structure as template (*14*). For each system, 5 replicas were simulated for a total of 1.0 μs using NAMD 3.0 (*37*). Trajectories were analyzed with VMD (*30*) and dynamical network analysis (*38*), which measures the correlation between the motions of neighboring residues to determine how cooperative their motion is. The higher the correlation between residues, the more relevant is their interaction for the stability of the protein complex (*39*). We determined contacts by tracking the distance between neighboring residues throughout the simulations, then selected the contacts with highest correlation for further analysis (see Supplementary Figure S10). Using these selection criteria, we identify the main contacts that are responsible for stabilizing the RBD:ACE2 complex (Figure 3A,B) and would thus be expected to have the greatest impact on the force-stability. All residues selected by the network analysis contact criterion are found within the receptor binding motif (RBM, residues N437 to Y508) region, at the RBD:ACE2 interface, defined as 4 Å cut-off based on the PDB ID 6m0j crystal structure (*40*) (see Supplementary Figure S11 for individual correlations). The total sum of correlations for RBD residues (Fig. 3C and Supplementary Figure S10) highlights mostly hydrophobic residues and also residues that are not mutated in the VOCs, revealing that stabilizing the bond between RBD:ACE2 involves an interplay of different interactions. Mutations in the VOCs lead to a rebalancing of interactions with ACE2, losing correlation in some regions while gaining in others (Figure 3C and Supplementary Figure S10).

Examining the specific mutations involved in the VOCs, we can rationalize the observed differences in force stability. Alpha carries only one substitution in the RBD, namely N501Y, which is also present in Beta and Gamma. The N501Y substitution creates an additional hydrogen bond and leads to increased pi-stacking with residue Y41 of ACE2 (*41*), which increases the pairwise correlation (Supplementary Figure S11 and S12) and enhances the correlations in the vicinity of position N501, in particular at residue T500 and G502 (Figure 3C).

The Beta and Gamma VOCs feature, in addition to N501Y, amino acid substitutions at position K417N/T and E484K. In the wt, the residues K417 and E484 form salt bridges with residues D30 and K31 of ACE2, respectively (*1*, *3*). Due to a charge-reversal in the case of E484K and a charge removal in the case of K417N (Beta) and K417T (Gamma), these salt bridges are disrupted. The disruption of the salt bridge at position 417 leads to dramatic loss in correlation (Figure 3C), fully in line with a dramatically decreased force stability for K417N (Figure 2B). The charge reversal by the mutation E484K leads to the loss of the salt bridge with K31, which is, however, compensated by an alternative salt bridge with E35 (*3*). As a result, the correlations around position E484 are virtually unaffected by the mutation (see e.g. residues F486, N487, Y489; Figure 3C), consistent with only a slight and statistically insignificant decrease in $F_{1/2}$ for the E484K mutation (Figure 2B). In summary, for the Beta and Gamma VOCs, the increased force stability by N501Y is offset by the reduction of stability in particular by K417N/T, such that the total effect is a similar force stability as wt.

The mutations in the Delta VOC, L452R and T478K, are located further away from the RBD:ACE2 interface, and there are no direct interactions involving these residues. Nonetheless, the Delta mutations do shift the correlation pattern, with correlations in the “Patch 2” region (Figure 3B) around position N501 decreasing and increasing in the region “Patch 1” around P479.

To summarize the contact network and the correlations of motion in a single metric to provide an overall measure of mechanical stability and to directly compare to the experimental force stability measurements, we define the total correlation as the sum of all correlations between stable contacts identified through the network analysis. We simulate the wt, the experimentally examined VOCs, and also the more recently emerged Omicron VOC and compute total correlation scores, using a bootstrapping approach to

determine confidence intervals (Figure 3D and Supplementary Figure S13). We find excellent agreement between the total correlation metric and the experimentally determined values for the force stability assessed by $F_{1/2}$: wt, Beta, Gamma, and Delta exhibit the same force stabilities, while Alpha has a statistically larger $F_{1/2}$ and total correlation. Interestingly, the recent Omicron variant, which features a very large number of mutations (15 in the RBD alone; (*42*)), has a total correlation value between Alpha and the wt, and did not show statistically significant differences when compared to Alpha and wt.

Discussion

We have used our tethered ligand assay and exploited the high sensitivity of MT and their ability to measure at constant forces to precisely determine both the force stability and affinity of different SARS-CoV-2 VOCs binding to ACE2. Unlike traditional bulk affinity measurements, our assay provides additional insights into bond-stability and kinetics under mechanical load, mimicking the natural binding circumstances in the dynamic environment of the respiratory tract. We find that while the Alpha, Beta, Gamma, and Delta VOCs all have increased affinities to ACE2 compared to wt, only Alpha has higher force stability. Viral fitness depends on multiple factors, including cleavage and cell entry, replication, and viral packing and release (*43-48*). Correspondingly, the VOCs carry mutations in positions beyond the RBD. However, attachment to the host cell is a critical first step in viral infection and it is instructive to relate trends observed epidemiologically with our findings about the RBD:ACE2 interaction. The Alpha, Beta, and Gamma VOCs variants all emerged in the second half of 2020 and began to circulate widely in late 2020 and early 2021 (Supplementary Figure S1). In Europe and Northern America, Alpha, but not Beta or Gamma, quickly replaced the wt and became the dominant circulating variant (Supplementary Figure S1). At that time, there was no widespread population immunity in Northern America or Europe (Supplementary Figure S1), suggesting that Alpha, but not Beta or Gamma, has a significant advantage in a (largely) immune-naïve population. We speculate that the higher force stability of Alpha contributes to its epidemiologically observed higher transmissibility compared to wt, Beta, or Gamma. The Beta and Gamma variants became dominant in South Africa and Brazil (Supplementary Figure S1), in a setting where there was already significant population immunity through natural infections

(*49, 50*). The charge change mutations at positions K417 and E484 present in Beta and Gamma reduce the binding of certain neutralizing antibodies (*51*), but lower the force stability. Consequently, the Beta and Gamma appear to confer an advantage to the virus in populations with significant immunity, but not in an immune-naïve population. The Delta and Omicron VOCs became dominant globally in mid 2021 and early 2022, respectively, at a time where there was significant population immunity through both vaccinations and natural infections (Supplementary Figure S1). Both variants show immune escape (*33, 52-54*) and likely enhanced transmission through substitution at the S1/S2 cleavage site, yet no, or only slightly increased force stability (Figure 2B and Figure 3D) (*55-57*). These observations raise the possibility that a new variant might emerge that combines the fitness advantages present in Omicron with a higher force stability, which could make it even more transmissible. Our correlation based analysis of the RBD:ACE2 interface by MD simulations and high-resolution force spectroscopy measurements of the interface in the tethered ligand assay has the potential to help understand and ultimately predict the spread of SARS-CoV-2 variants.

ACKNOWLEDGMENTS

We thank Meike Bos, Joost de Graf, and David Dulin for helpful discussions and Leonard Schendel, Nina Beier, Benedikt Böck, Ellis Durner, Stefanie D. Pritzl, and Caroline Körösy for help with experiments. This study was supported by German Research Foundation Projects 386143268 and 111166240, a Human Frontier Science Program Cross Disciplinary Fellowship (LT000395/2020C) and European Molecular Biology Organization Non-Stipendiary long-term fellowship (ALTF 1047-2019) to L.F.M., and the Physics Department of LMU Munich. R.C.B., M.C.R.M., and P.S.F.C.G. are supported by start-up funds provided by Auburn University.

WHO name	**Pango lineage**	**Country of first observation**	**aa changes in RBD**	**$F_{1/2}$ (pN)** ($F_{1/2}/F_{1/2}$(wt)) > 1: Higher force-stability than wt	**$\tau_{0,diss}$ (s)** ($t_{0,diss}/t_{0,diss}$(wt)) < 1: Faster binding than wt at F = 0	**$\tau_{0,bound}$ (s)** ($t_{0,bound}/t_{0,bound}$(wt)) > 1: Slower dissociation than wt at F = 0	**K_D** (K_D/K_D(wt)) < 1: Higher affinity than wt
wt	A	-	-	3.8 ± 0.4 (1)	0.06 ± 0.17 (1)	121 ± 284 (1)	$532 \cdot 10^{-6}$ (1)
Alpha	B1.1.7	UK	N501Y	4.5 ± 0.3 (1.17)	0.01 ± 0.02 (0.22)	464 ± 740 (3.82)	$30 \cdot 10^{-6}$ (0.06)
Beta	B1.1.351	South Africa	N501Y E484K K417N	3.8 ± 0.3 (1.01)	0.02 ± 0.06 (0.37)	218 ± 315 (1.79)	$110 \cdot 10^{-6}$ (0.21)
Gamma	P1	Brazil	N501Y E484K K417T	4.0 ± 0.6 (1.06)	0.02 ± 0.04 (0.27)	552 ± 1178 (4.55)	$31 \cdot 10^{-6}$ (0.06)
Delta	B1.617.2	India	L452R T478K	3.8 ± 0.3 (1.00)	0.01 ± 0.02 (0.18)	427 ± 707 (3.52)	$27 \cdot 10^{-6}$ (0.05)

Table 1. VOCs compared to SARS-CoV-2 wt. Number of molecules: 13 molecules (wt), 11 molecules (Alpha), 10 molecules (Beta), 14 molecules (Gamma), 20 molecules (Delta).

References

1. C. Laffeber, K. d. Koning, R. Kanaar, J. H. G. Lebbink, Experimental Evidence for Enhanced Receptor Binding by Rapidly Spreading SARS-CoV-2 Variants. *J Mol Biol* **433**, 167058-167058 (2021).
2. M. I. Barton *et al.*, Effects of common mutations in the SARS-CoV-2 Spike RBD and its ligand, the human ACE2 receptor on binding affinity and kinetics. *Elife* **10**, e70658 (2021).
3. D. B. Hill *et al.*, Force Generation and Dynamics of Individual Cilia under External Loading. *Biophysical Journal* **98**, 57-66 (2010).
4. C.-T. Wu *et al.*, SARS-CoV-2 Replication in Airway Epithelia Requires Motile Cilia and Microvillar Reprogramming. *Ssrn Electron J*, (2022).
5. L. F. Milles, K. Schulten, H. E. Gaub, R. C. Bernardi, Molecular mechanism of extreme mechanostability in a pathogen adhesin. *Science* **359**, 1527-1533 (2018).
6. D. Alsteens *et al.*, Nanomechanical mapping of first binding steps of a virus to animal cells. *Nature Nanotechnology* **12**, 177-183 (2017).
7. M. Koehler, M. Delguste, C. Sieben, L. Gillet, D. Alsteens, Initial Step of Virus Entry: Virion Binding to Cell-Surface Glycans. *Annual Review of Virology* **7**, null (2020).
8. E. V. Sokurenko, V. Vogel, W. E. Thomas, Catch-Bond Mechanism of Force-Enhanced Adhesion: Counterintuitive, Elusive, but … Widespread? *Cell Host Microbe* **4**, 314-323 (2008).
9. F. Tian *et al.*, N501Y mutation of spike protein in SARS-CoV-2 strengthens its binding to receptor ACE2. *Elife* **10**, e69091 (2021).
10. B. Zheng *et al.*, S373P Mutation of Spike Protein in SARS-CoV-2 Stabilizes Omicron. *bioRxiv*, 2022.2006.2022.497114 (2022).
11. M. Koehler *et al.*, Molecular insights into receptor binding energetics and neutralization of SARS-CoV-2 variants. *Nature Communications* **12**, 6977 (2021).
12. X. Zhang *et al.*, Pathogen-host adhesion between SARS-CoV-2 spike proteins from different variants and human ACE2 studied at single-molecule and single-cell levels. *Emerg Microbes Infec* **11**, 2658-2669 (2022).
13. R. Zhu *et al.*, Force-tuned avidity of spike variant-ACE2 interactions viewed on the single-molecule level. *Nat Commun* **13**, 7926 (2022).
14. M. S. Bauer *et al.*, A tethered ligand assay to probe SARS-CoV-2:ACE2 interactions. *Proc National Acad Sci* **119**, (2022).
15. A. Löf *et al.*, Multiplexed protein force spectroscopy reveals equilibrium protein folding dynamics and the low-force response of von Willebrand factor. *Proc National Acad Sci*, 201901794 (2019).
16. B. M. Lansdorp, O. A. Saleh, Power spectrum and Allan variance methods for calibrating single-molecule video-tracking instruments. *Rev Sci Instrum* **83**, 025115 (2012).
17. A. J. W. t. Velthuis, J. W. J. Kerssemakers, J. Lipfert, N. H. Dekker, Quantitative Guidelines for Force Calibration through Spectral Analysis of Magnetic Tweezers Data. *Biophys J* **99**, 1292-1302 (2010).
18. K. C. Neuman, A. Nagy, Single-molecule force spectroscopy: optical tweezers, magnetic tweezers and atomic force microscopy. *Nat Methods* **5**, 491-505 (2008).
19. J. Lipfert, X. Hao, N. H. Dekker, Quantitative Modeling and Optimization of Magnetic Tweezers. *Biophys J* **96**, 5040-5049 (2009).

20. M. S. Bauer *et al.*, A Tethered Ligand Assay to Probe the SARS-CoV-2 ACE2 Interaction under Constant Force. *Biorxiv*, 2020.2009.2027.315796 (2020).
21. W. Ott *et al.*, Elastin-like Polypeptide Linkers for Single-Molecule Force Spectroscopy. *Acs Nano* **11**, 6346 6354 (2017).
22. J. Kim, C. Z. Zhang, X. Zhang, T. A. Springer, A mechanically stabilized receptor-ligand flex-bond important in the vasculature. *Nature* **466**, 992-995 (2010).
23. P. Shrestha *et al.*, Single-molecule mechanical fingerprinting with DNA nanoswitch calipers. *Nature Nanotechnology* **84**, 1-9 (2021).
24. D. Yang, A. Ward, K. Halvorsen, W. P. Wong, Multiplexed single-molecule force spectroscopy using a centrifuge. *Nature communications* **7**, 11026 (2016).
25. F. Kilchherr *et al.*, Single-molecule dissection of stacking forces in DNA. *Science* **353**, aaf5508 (2016).
26. S. Le, M. Yu, J. Yan, Direct single-molecule quantification reveals unexpectedly high mechanical stability of vinculin—talin/α-catenin linkages. *Sci Adv* **5**, eaav2720 (2019).
27. K. Halvorsen, D. Schaak, W. P. Wong, Nanoengineering a single-molecule mechanical switch using DNA self-assembly. *Nanotechnology* **22**, 494005 (2011).
28. D. Kostrz *et al.*, A modular DNA scaffold to study protein-protein interactions at single-molecule resolution. *Nat Nanotechnol* **14**, 988-993 (2019).
29. S. Y. Gong *et al.*, Contribution of single mutations to selected SARS-CoV-2 emerging variants spike antigenicity. *Virology* **563**, 134-145 (2021).
30. M. M. Rajah *et al.*, SARS-CoV-2 Alpha, Beta, and Delta variants display enhanced Spike-mediated syncytia formation. *Embo J* **40**, e108944 (2021).
31. S. M. C. Gobeil *et al.*, Effect of natural mutations of SARS-CoV-2 on spike structure, conformation, and antigenicity. *Science* **373**, (2021).
32. W. Ren *et al.*, Characterization of SARS-CoV-2 Variants B.1.617.1 (Kappa), B.1.617.2 (Delta), and B.1.618 by Cell Entry and Immune Evasion. *Mbio* **13**, e00099-00022 (2022).
33. M. McCallum *et al.*, Molecular basis of immune evasion by the Delta and Kappa SARS-CoV-2 variants. *Science* **374**, 1621-1626 (2021).
34. C. Albrecht *et al.*, DNA: A programmable force sensor. *Science* **301**, 367 370 (2003).
35. S. Gruber *et al.*, Designed anchoring geometries determine lifetimes of biotin–streptavidin bonds under constant load and enable ultra-stable coupling. *Nanoscale* **12**, 21131-21137 (2020).
36. B. Webb, A. Sali, Comparative Protein Structure Modeling Using MODELLER. *Curr Protoc Bioinform* **54**, 5.6.1-5.6.37 (2016).
37. J. C. Phillips *et al.*, Scalable molecular dynamics on CPU and GPU architectures with NAMD. *J Chem Phys* **153**, 044130 (2020).
38. M. C. R. Melo, R. C. Bernardi, C. d. l. Fuente-Nunez, Z. Luthey-Schulten, Generalized correlation-based dynamical network analysis: a new high-performance approach for identifying allosteric communications in molecular dynamics trajectories. *J Chem Phys* **153**, 134104 (2020).
39. C. Schoeler *et al.*, Mapping Mechanical Force Propagation through Biomolecular Complexes. *Nano Lett* **15**, 7370-7376 (2015).
40. J. Lan *et al.*, Structure of the SARS-CoV-2 spike receptor-binding domain bound to the ACE2 receptor. *Nature* **581**, 215-220 (2020).

41. H. Liu *et al.*, The basis of a more contagious 501Y.V1 variant of SARS-CoV-2. *Cell Res* **31**, 720-722 (2021).
42. P. Han *et al.*, Receptor binding and complex structures of human ACE2 to spike RBD from omicron and delta SARS-CoV-2. *Cell* **185**, 630-640.e610 (2022).
43. J. Shang *et al.*, Cell entry mechanisms of SARS-CoV-2. *Proc National Acad Sci* **117**, 11727-11734 (2020).
44. P. V'kovski, A. Kratzel, S. Steiner, H. Stalder, V. Thiel, Coronavirus biology and replication: implications for SARS-CoV-2. *Nat Rev Microbiol*, 1-16 (2020).
45. W. A. Michaud, G. M. Boland, S. A. Rabi, The SARS-CoV-2 Spike mutation D614G increases entry fitness across a range of ACE2 levels, directly outcompetes the wild type, and is preferentially incorporated into trimers. *Biorxiv*, 2020.2008.2025.267500 (2020).
46. C. B. Jackson, M. Farzan, B. Chen, H. Choe, Mechanisms of SARS-CoV-2 entry into cells. *Nat Rev Mol Cell Bio* **23**, 3-20 (2022).
47. W. T. Harvey *et al.*, SARS-CoV-2 variants, spike mutations and immune escape. *Nat Rev Microbiol* **19**, 409-424 (2021).
48. A. Escalera *et al.*, Mutations in SARS-CoV-2 variants of concern link to increased spike cleavage and virus transmission. *Cell Host Microbe* **30**, 373-387.e377 (2022).
49. L. F. Buss *et al.*, Three-quarters attack rate of SARS-CoV-2 in the Brazilian Amazon during a largely unmitigated epidemic. *Sci New York N Y* **371**, 288-292 (2021).
50. K. Sun *et al.*, SARS-CoV-2 transmission, persistence of immunity, and estimates of Omicron's impact in South African population cohorts. *Sci Transl Med*, eabo7081 (2022).
51. T. N. Starr *et al.*, Deep Mutational Scanning of SARS-CoV-2 Receptor Binding Domain Reveals Constraints on Folding and ACE2 Binding. *Cell* **182**, 1295-1310.e1220 (2020).
52. P. Mlcochova *et al.*, SARS-CoV-2 B.1.617.2 Delta variant replication and immune evasion. *Nature* **599**, 114-119 (2021).
53. J. Hu *et al.*, Increased immune escape of the new SARS-CoV-2 variant of concern Omicron. *Cell Mol Immunol* **19**, 293-295 (2022).
54. B. Ju *et al.*, Immune escape by SARS-CoV-2 Omicron variant and structural basis of its effective neutralization by a broad neutralizing human antibody VacW-209. *Cell Res* **32**, 1-4 (2022).
55. Y. Fan *et al.*, SARS-CoV-2 Omicron variant: recent progress and future perspectives. *Signal Transduct Target Ther* **7**, 141 (2022).
56. D. Planas *et al.*, Considerable escape of SARS-CoV-2 Omicron to antibody neutralization. *Nature* **602**, 671-675 (2022).
57. B. Li *et al.*, Viral infection and transmission in a large, well-traced outbreak caused by the SARS-CoV-2 Delta variant. *Nature communications* **13**, 460 (2022).

FIGURES

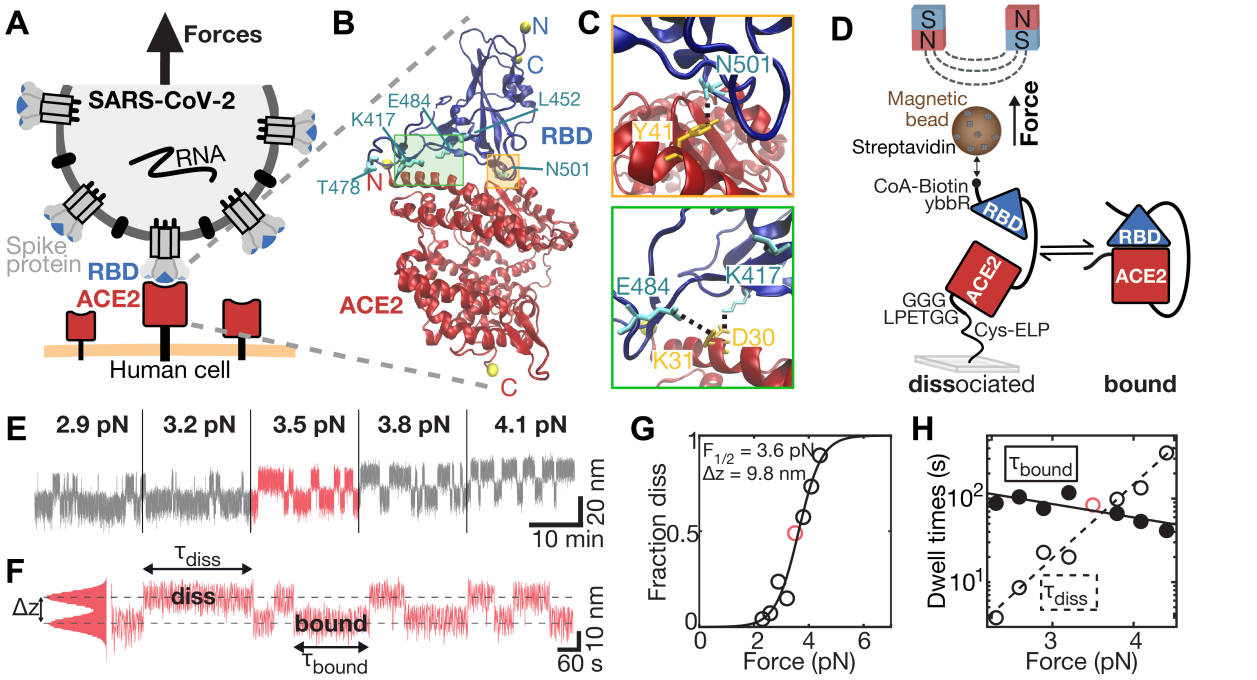

Figure 1: A single-molecule tethered ligand assay to study RBD binding to ACE2 for variants of concern of SARS-CoV-2. A A SARS-CoV-2 virion (grey) presents its spike protein trimers containing three RBDs (blue) ready for binding to human ACE2 (red). Attachment occurs in the dynamic environment of the respiratory tract, where the interaction must withstand external forces (black arrow). **B** Crystal structure of SARS-CoV-2 RBD (blue) bound to ACE2 (red) (PDB ID: 6m0j) (*1*). Termini of protein chains are marked with yellow spheres. Amino acid substitutions featured in current variants of concern (VOCs) are indicated in cyan. Crystal structure was rendered using VMD (*2*). **C** Zooms into the interface regions indicated in **B**. Top: RBD residue N501 featured in VOCs Alpha, Beta, and Gamma forms a hydrogen-bond with ACE2 residue Y41 (*1*). Bottom: RBD residues E484 and K417 featured in VOCs Beta and Gamma form salt bridges and hydrogen bonds with ACE2 residues K31 and D30 respectively (*1*, *3*). Bridges and bonds are indicated as black dashed lines. **D** Schematic representation of the tethered ligand construct in MT. SARS-CoV-2 RBD (blue) is tethered via a flexible peptide linker to ACE2 (red). The construct is covalently attached to the glass surface via an ELP linker (see Materials and Methods), and to a streptavidin-covered magnetic bead via biotin at the C-terminus of the protein construct. **E** Representative extension time trace of the tethered ligand construct in MT shows binding and dissociation of the SARS-CoV-2 RBD:ACE2 interaction at plateaus of constant force. With increasing force, the interface is predominantly dissociated. **F** Segment of the trace in **E** at 3.5 pN, where it is equally distributed between the bound and dissociated ("diss") state. The fraction dissociated at this force is thus 0.5. Lifetimes in the dissociated state (τ_{diss}) and in the bound state (τ_{bound}) are indicated. **G** Fraction dissociated as a function of applied force (circles) and fit of a two-state model (solid line), with $F_{1/2}$ and Δz (inset) as fitting parameters. **H** Mean lifetimes in the bound and dissociated state for the molecule shown in E-G as a function of force (circles) and fit with an exponential model (solid lines).

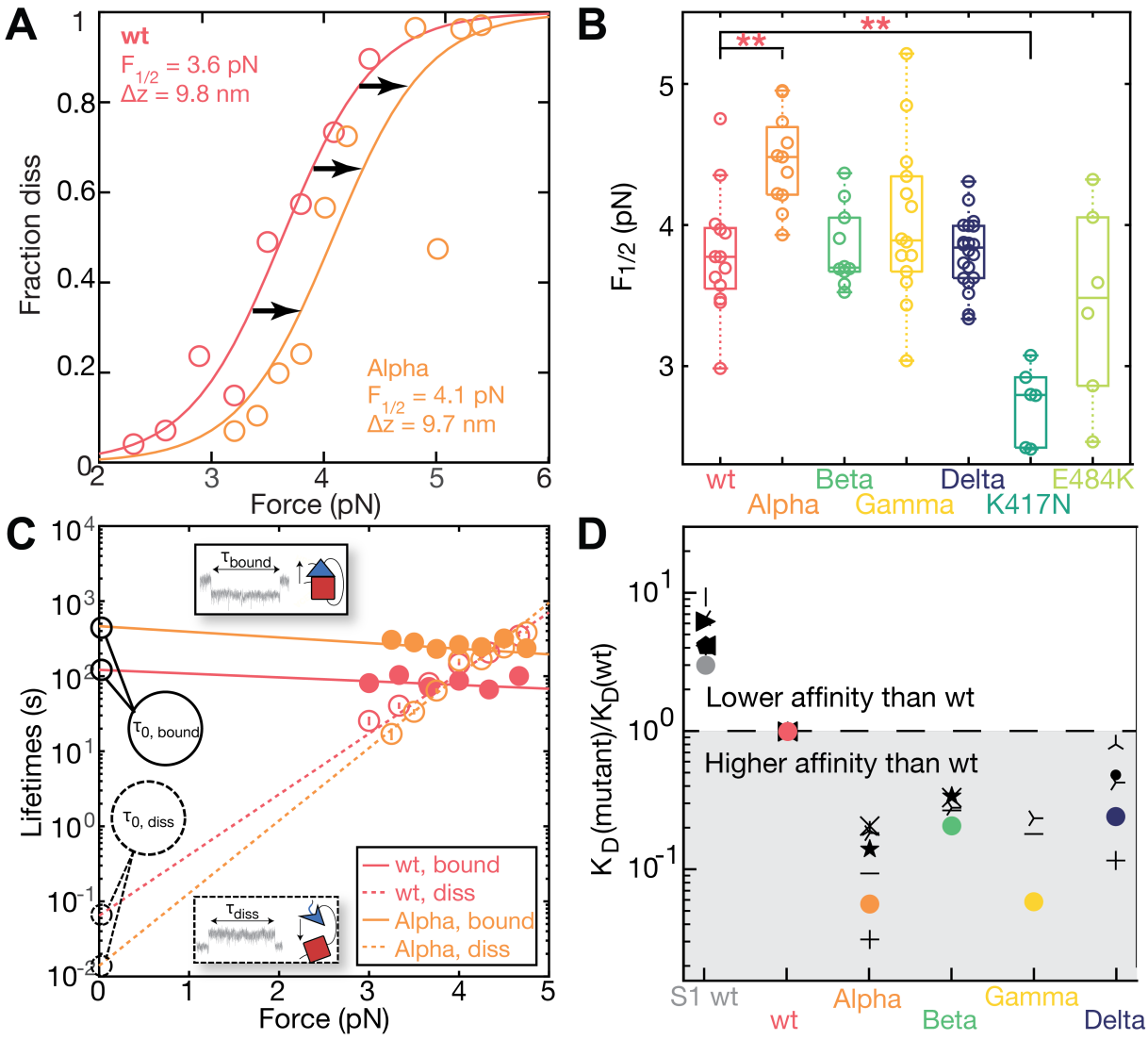

Figure 2: Effects of VOCs on interface force stability and affinity. A Representative force-dependent fraction dissociated for one single wt (red), and one Alpha (orange) tethered ligand construct. Points represent experimental data and solid lines two-state fits. Additional data are in Supplementary Figure S5. **B** Midpoint forces determined for wt, VOCs, and K417N, and E484K single amino acid substitutions. $F_{1/2}$ of Alpha and K417N deviate highly significantly from wt (p-values p = 0.00052 and p = 0.000045, respectively). Beta, Gamma, Delta, and E484K show no statistically significant difference to the wt. A bootstrap analysis revealed similar significance levels for the different variants (Supplementary Figure S6). Individual points are derived from independent molecules. Boxes indicate the median, 25th and 75th percentile. Numerical data are provided in Supplementary Table S1. **C** Force-dependent lifetimes (circles) and fits to the data in the bound (solid lines) and dissociated (dashed) state of wt and Alpha. Individual points are the means of lifetimes observed for a single molecule at a given force. Insets show example lifetimes

in MT traces. Additional comparisons for the other VOCs are in Supplementary Figure S7. **D** Mean dissociation constant normalized to the wt (K_D/K_D(wt); unnormalized K_Ds are in Supplementary Figure S9) determined from our measurements (colored dots) and compared to previous traditional bulk affinity measurements (SPR or BLI) (*3*–*9*) (Supplementary Table T2). Statistics in panels **B** - **C** reflect 13 molecules (wt), 11 molecules (Alpha), 10 molecules (Beta), 14 molecules (Gamma), 20 molecules (Delta), 6 molecules (E484K), and 6 molecules (K417N).

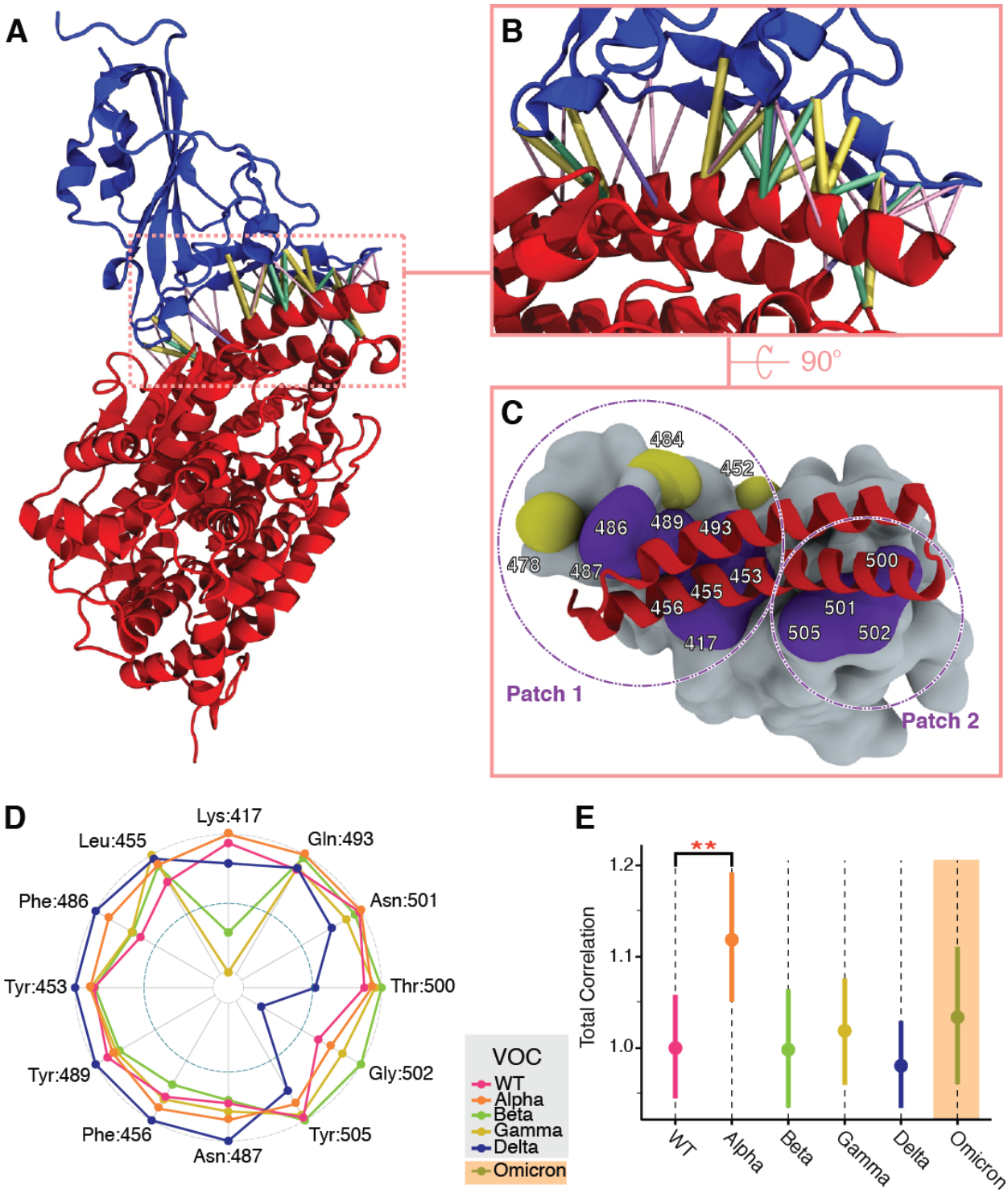

Figure 3: Effects of VOCs on the contact network at RBD:ACE2 interface. A Network interactions between Spike RBD (blue) in complex with ACE2 (red) of an exemplary MD trajectory represented as color coded cylinders according to their correlation, where thicker cylinders in yellow and green represent highly correlated residues. Less correlated residues are depicted in light and dark purple and thin lines. **B** Zoom into the structure shown in panel A, focusing on the

RBD:ACE2 interface. **C** Detailed RBD:ACE2 surface interface highlighting the receptor binding domain (RBD) in grey and ACE2 helices in red. Residues colored in violet are highly correlated while residues colored in yellow are less correlated. **D** Total correlations for selected residues for the different VOCs. Values are normalized to the VOC with the strongest correlation. **E** Total correlation of motion summarized from the dynamic network interactions of all main correlations across the RBD:ACE2 interface, for each VOC. Total correlation measurements for all variants were normalized by the mean total correlation in the WT. Bars represent the 90% confidence intervals for the mean. The Alpha VOC shows a significantly higher correlation than wt (two stars represent a significance level $p < 0.05$). All other VOCs are not significantly different from wt. For additional significance tests via bootstrapping see Supplementary Figure S13.